16 (2022) 100130

Contents lists available at ScienceDirect

Journal of Non-Crystalline Solids: X

journal homepage: www.sciencedirect.com/journal/journal-of-non-crystalline-solids-x

Deformation behaviors of a model metallic glass under 3-D nanoindentation studied in molecular dynamics simulation

Haidong Liu, Yunfeng Shi, Liping Huang *

Department of Materials Science and Engineering, Rensselaer Polytechnic Institute, Troy, NY 12180, USA

ARTICLE INFO

Keywords:
Metallic glass
Nanoindentation
Shear band formation
Crack
Deformation
Molecular dynamics simulations

ABSTRACT

In recent years, molecular dynamics (MD) simulation has been used to study the deformation behaviors of glass under nanoindentation, mainly using ideal geometries like a spherical indenter or a 2.5-D sample geometry to simplify post-analysis and save computational costs. To generate stress/strain fields that can be directly compared with experiments, we developed a 3-D nanoindentation protocol in this work to study the deformation behaviors of a model metallic glass under sharp contact loading in MD. Our studies show that the indenter sharpness controls the shear band formation, and the interaction between shear bands dictates the crack initiation in the model metallic glass. Shear bands and residual stress fields in the model metallic glass from our simulated nanoindentation tests are consistent with observations in soda-lime silicate (SLS) glass from the instrumented indentation in experiments, as both of them favor shear deformation under sharp contact loading.

1. Introduction

Damage under sharp contact loading is one of the primary failure modes in glasses [1]. For decades, researchers have been applying and improving the instrumented indentation to mimic and study this type of damage. However, it is very challenging to understand the deformation behaviors of glass under sharp contact loading as the deformation modes depend on various factors, such as glass compositions and surface conditions, testing temperature and atmosphere, indenter shape and sharpness [2–13]. Furthermore, unraveling the nature of structural changes under indentation is a formidable task because of the complexity that originates from the atomic-scale disorder of glass and the experimental difficulties associated with *in-situ* investigations at a local scale (tens of microns) under non-uniform stress fields [7,14]. To this end, nanoindentation tests simulated by MD have been well-adapted to study glass deformation at the atomic level [15]. Many simulated nanoindentation tests have been reported in recent years to advance the understanding of the deformation and cracking behaviors of glass under indentation [16–24]. Yuan et al. used the simulated nanoindentation in MD to compare deformation modes in densified and pristine silica glass [17]. Yang et al. investigated the crack formation criteria in a model metallic glass system [18]. Liu et al. illustrated the role of boron in improving the crack resistance of glasses with high boron contents [20]. Lee et al. reported that embedding nanoparticles in glass could deflect the crack propagation to increase the crack resistance of glass [19]. Besides tuning glass structure and compositions, Zhao et al. used the simulated nanoindentation to investigate the effects of pre-stress on deformation behaviors and shear bands forming morphologies in metallic glass under indentation [21]. Most nanoindentation tests in MD adopted a so-called "2.5-D" setup that reduces one of the lateral sample dimensions and the complexity of the stress and strain fields during indentation, thus the computational cost. However, the thin-slab geometry cannot generate stress/strain fields and crack patterns that can be directly compared with the instrumented indentation tests in experiments or in real-life scenarios [20]. There are few simulated nanoindentation tests in MD using a 3-D approach that is similar to the experiment setup. Kilymis et al. studied radiation damage on structural and mechanical properties of nuclear waste glasses under 3-D nanoindentation [25–27]. Nomura et al. investigated the migration and recombination of defect states in silica glass under 3-D nanoindentation [28]. However, none of these simulated 3-D nanoindentation studies in MD focused on crack initiation and propagation in glass under sharp contact loading.

This study reports the development and application of a 3-D nanoindentation method in MD simulations to investigate the deformation behaviors of glass under sharp contact loading. A model metallic glass [29] favoring shear flow deformation was used throughout this study. Activation and propagation of different shear band systems in the model

* Corresponding author.
E-mail address: huangL5@rpi.edu (L. Huang).

https://doi.org/10.1016/j.nocx.2022.100130
Received 22 September 2022; Received in revised form 1 November 2022; Accepted 5 November 2022
Available online 7 November 2022

glass were observed under 3-D nanoindentation tests in MD using indenters with different tip angles and correlated to the evolution of glass structure and stress fields underneath the indenter. Results from our simulated 3-D nanoindentation tests in the model metallic glass were compared favorably with several experimental studies in metallic glasses and in soda-lime silicate (SLS) glass that also favors shear deformation under indentation [9–12,30–33]. Our studies demonstrate that 3-D nanoindentation tests in MD can serve as an important tool to understand the deformation and cracking behaviors of glass under sharp contact loading and provide insights for designing damage resistant glasses.

2. Method

2.1. Sample preparation

In this work, a modified Lennard-Jones (BLJ) potential [29] was used to model the response of a binary metallic glass to sharp contact loading in simulated 3-D nanoindentation tests in MD. This computationally efficient potential can be tuned to make the model BLJ metallic glass more brittle to facilitate crack formation under indentation [18]. The function forms of the potential are shown in Eq. 1.

$$\varphi_{BLJ}(r) = \begin{cases} \varphi_{LJ}(r), \text{for } r < r_{\alpha\beta}^{S} \\ \varphi_{LJ}(r) + \varepsilon_B \varepsilon_{LL} \, sin^2\left(\pi \dfrac{r_{\alpha\beta}^{C} - r}{r_{\alpha\beta}^{C} - r_{\alpha\beta}^{S}}\right), \text{for } r \geq r_{\alpha\beta}^{S} \\ 0, \text{for } r \geq r^{C} \end{cases} \quad (1)$$

where $\varphi_{LJ}(r) = 4\varepsilon_{\alpha\beta}\left(\frac{\sigma_{\alpha\beta}^{12}}{r^{12}} - \frac{\sigma_{\alpha\beta}^{6}}{r^{6}}\right) - \varepsilon_{cutoff}$, $\varepsilon_{\alpha\beta}$ and $\sigma_{\alpha\beta}$ are the energy scale and length scale of the pair interactions. The model BLJ glass consists of an equal amount of large and small atoms with $m_L = 2m_0$, $m_S = m_0$. All bonds have the same strength but different lengths: $\varepsilon_{LL} = \varepsilon_{LS} = \varepsilon_{SS}$; $\sigma_{SS} = \left(\frac{5}{6}\right)\sigma_{LL}$, $\sigma_{LS} = \left(\frac{11}{12}\right)\sigma_{LL}$. The cutoffs are determined by having identical interactions at the cutoff for all pairs and only including the nearest neighbor interactions: $r_{LL}^{C} = 1.4\sigma_{LL}$, $r_{LS}^{C} = 1.2833\sigma_{LL}$, $r_{SS}^{C} = 1.1667\sigma_{LL}$. This model BLJ glass is close to the $Ni_{50}Nb_{50}$ metallic glass in terms of composition and atomic radius ratio [29]. The bump height ε_B, which can vary from 0 for a ductile sample to 0.8 for a brittle sample as shown in Fig. 1. A higher ε_B value leads to a higher elastic modulus, a higher yield strength and a smaller failure strain in a uniaxial tensile test as shown in Fig. 1(b). In this study, $\varepsilon_B = 0.8$ was used to promote crack formation in a brittle sample. A sample consisting of 80,000 atoms was prepared from high-temperature liquid equilibrated at 2105 K and then quenched isochorically to 5 K with a cooling rate of 0.83 K/ps using the Nose-Hover thermostat. A standard Velocity Verlet integrator in LAMMPS with KOKKOS acceleration package was used with a timestep of 5 fs for all simulations in this work [34,35]. Glass transition temperature of this model metallic glass is around 900 K, largely insensitive to the bump height [29]. The sample was relaxed under zero pressure at 5 K in an NPT ensemble using the Nose-Hover thermostat and Nose-Hover barostat [36]. The relaxed sample (14.3 nm × 14.3 nm × 6.2 nm) was then duplicated to prepare large samples for simulated nanoindentation tests using different indenter angles in the rest of the work. Due to the inhomogeneous stress fields under nanoindentation, the artificial periodicity in the sample will not lead to any periodicity in the mechanical response of glass to sharp contact loading.

2.2. Nanoindentation setup

A schematic of the 3-D nanoindentation setup in MD simulation is shown in Fig. 2. Sample sizes are different for different indenters to ensure that the far-field stress does not create appreciable effects on local deformations underneath the indenter. Periodic boundary conditions were kept along lateral dimensions, and stresses along the two lateral dimensions were set to zero. Unlike other 3-D nanoindentation studies in MD [25,27,28,37], a reflective wall was placed underneath the sample, allowing atoms to relax along the lateral dimensions but restricting them from moving beyond the bottom, thus promoting the crack formation under indentation [18]. A hollow indenter consists of several layers of rigid carbon atoms with a diamond cubic structure (Fig. 2(a)), interacting with the glass sample atoms via the ZBL potential [38]. The indenter has a pyramidal shape similar to the Vickers indenter, characterized by its apex angle and a tip radius of 5 nm. The indenter approaches the sample at a speed of 20 m/s to reach a depth of about 30–50 nm until the sample develops significant plastic deformation. Simulated nanoindentation was either continued loading to observe the shear band development or unloading to study the residual stress. Dimensions of samples studied in nanoindentation tests using different indenter angles are shown in Table 1.

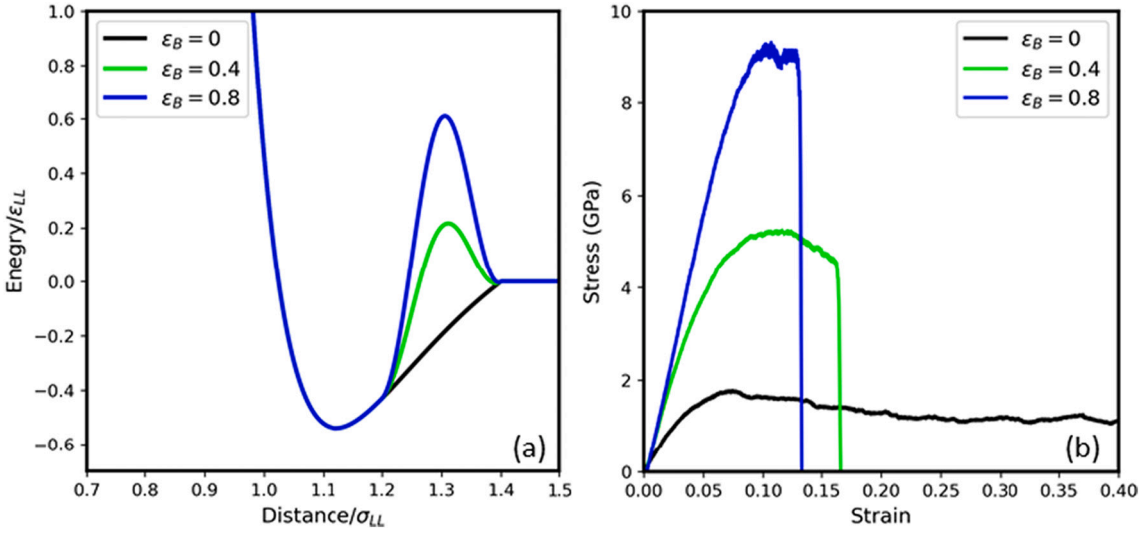

Fig. 1. (a) Potential energy versus atomic distance and (b) stress-strain curves from uniaxial tensile tests in BLJ samples with different bump heights indicated by the ε_B values in legends [29].

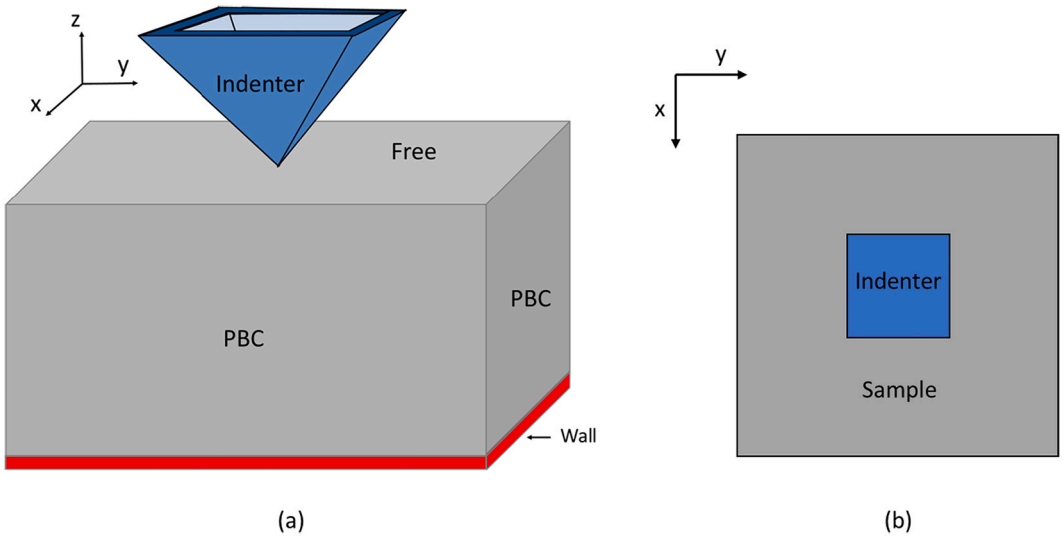

Fig. 2. (a) Side view and (b) top view of the 3-D nanoindentation setup in MD simulations in this work.

Table 1
Dimensions and total number of atoms in samples studied in nanoindentation tests using different indenter angles.

Indenter Angle	Dimension x (nm)	Dimension y (nm)	Dimension z (nm)	Total number of atoms
60°	161.5	161.5	218.4	338,800,000
90°	234.9	234.9	175.5	471,040,000
120°	191.7	191.7	153.9	338,800,000

3. Results

3.1. Stress distribution

Unlike previous studies using the 2.5-D setup in the plane stress condition, it is challenging to analyze and visualize all of the stress components in 3-D nanoindentation. This study focuses on stress invariants instead of individual stress components, as the formers are usually used to formulate failure criteria in elastic-plastic materials and can reduce the complexity of stress analysis [39]. Instead of directly analyzing the atomic stress with significant fluctuations, stress components are averaged over spatial grids, which are used to calculate the stress invariants in each grid volume ($1.35 \times 1.35 \times 1.35$ nm^3) [18]. Stress invariants of I_1, I_2, and I_3 are calculated as follows:

$$I_1 = \sigma_{11} + \sigma_{22} + \sigma_{33} \tag{2}$$

$$I_2 = \sigma_{12}^2 + \sigma_{13}^2 + \sigma_{23}^2 - (\sigma_{11}\sigma_{22} + \sigma_{11}\sigma_{33} + \sigma_{22}\sigma_{33}) \tag{3}$$

$$I_3 = \sigma_{11}\sigma_{22}\sigma_{33} + 2\sigma_{12}\sigma_{23}\sigma_{31} - \sigma_{12}^2\sigma_{33} - \sigma_{23}^2\sigma_{11} - \sigma_{13}^2\sigma_{22} \tag{4}$$

The interpretation of I_1 is the most straightforward, where a positive and negative value indicate a tensile and compressive hydrostatic stress state, respectively. The interpretation of I_2 can be viewed as an indicator of the nature of the dominated stress state, where a positive and negative sign indicate a predominant shear and hydrostatic stress state, respectively. The interpretation of I_3 is not straightforward, and we will explain it in the Discussion section.

Maps of stress invariants during loading before substantial shear band development underneath the indenter are shown in Fig. 3. The hydrostatic tensile (red) and compressive (blue) stress distribution represented by I_1 in the top row of Fig. 3 is consistent with other studies, and highly affected by the indenter sharpness [23,40,41]. As the indenter angle increases, the magnitude and the spatial distribution of tensile stress underneath the indenter decrease, while a larger area around the indenter builds up a higher magnitude of compressive stress. As indicated by I_2 in the middle row of Fig. 3, the dominated stress state transitions from hydrostatic (blue) to shear (red) around the indenter regardless of the indenter angle. Due to the higher tensile stress under the 60° indenter, there is another small area with a hydrostatic stress state below the region with a predominant shear stress state. I_3 in the bottom row of Fig. 3 shows the most interesting pattern, where a narrow band of the positive sign occurs between regions of the negative sign. This band appears in the transition zone in I_2 and coincides with the crack initiation shown in Fig. 8 later. The effect of the indenter sharpness is also very obvious in I_2 and I_3 in terms of their spatial distribution and shapes of the regions with different signs.

3.2. Shear band formation

Atomic shear strain underneath the indenter was analyzed and shown in Fig. 4. Metallic glass usually deforms plastically through shear band formation [15,42], which is observed in this study for all three indenter angles. Fig. 4 shows that the shear deformation is localized nearer to the indenter tip for a sharper indenter, which is consistent with the observations in a previous finite element study [43]. Shear bands form at different indentation depths and develop in different directions under nanoindentation tests using different indenter angles. Between 60° and 120° nanoindentation tests, the shear bands develop in opposite directions such that the shear band propagates upwards toward the sample surface under the 60° nanoindentation, while the ones underneath the 120° nanoindentation propagate downwards. Both types of shear bands develop simultaneously in the 90° nanoindentation.

The load-displacement curves are shown in Fig. 5 for simulated nanoindentation tests using different indenters. The formations of the shear band in Fig. 4 are consistently correlated with kinks on the load-displacement curves, which agree with previous experimental studies where the serrations on the load-displacement curves come from the serrated flow [9–11,44]. Similar to experimental observations [9], Fig. 5 shows that the sharper the indenter, the more obvious the kinks on the load-displacement curves, and at a deeper indentation depth they start to appear.

To illustrate the formation of the two types of shear bands in Fig. 4, we focus on the faces of the indenter where the plane normal directions are indicated as black arrows in Fig. 6. The effect of the indenter face can be viewed as a simple compression perpendicular to the sample combined with a frictional force. There are two shear directions at roughly 45° from the plane normal to the indenter face, and shear bands

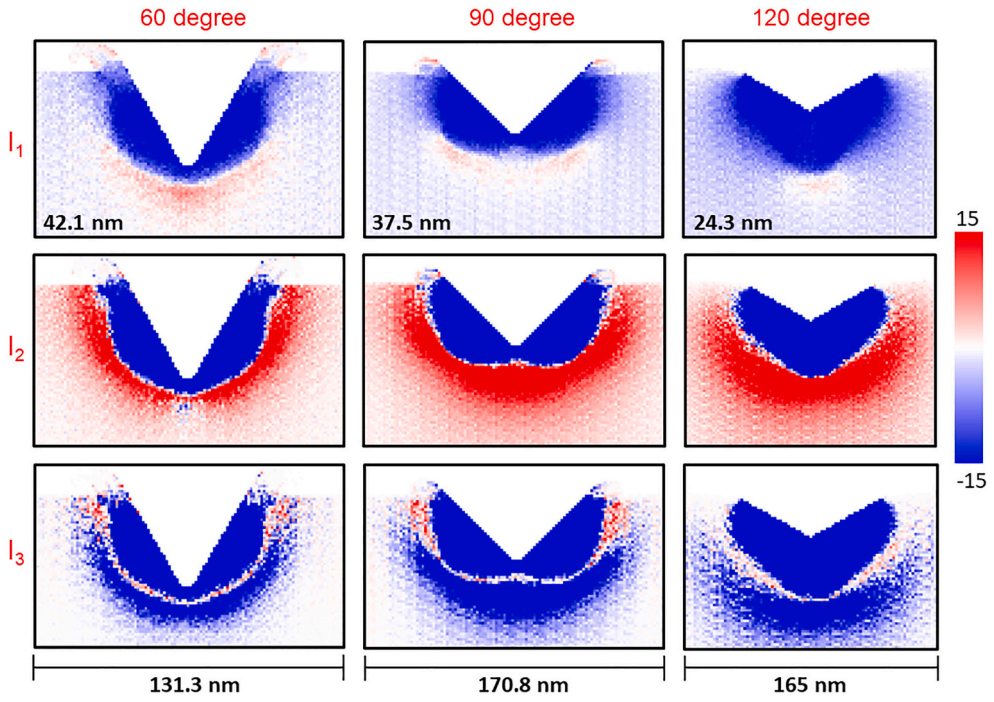

Fig. 3. Stress invariants of I_1, I_2, and I_3 during loading in 60°, 90°, and 120° nanoindentation at depths of 42.1, 37.5, and 24.3 nm, respectively, where I_1 is in GPa.

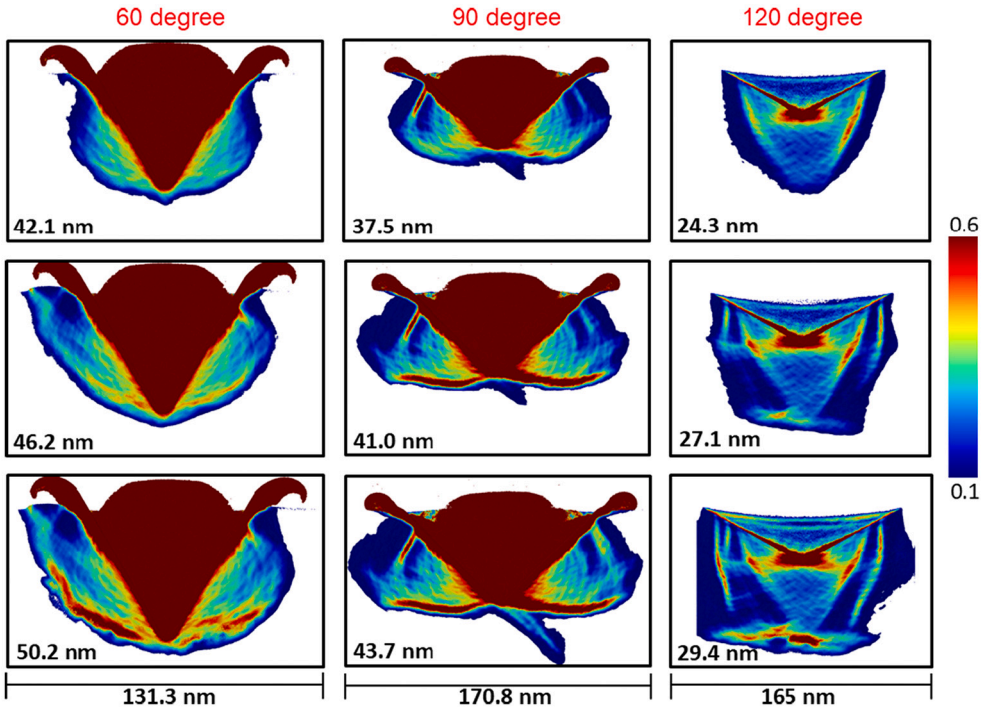

Fig. 4. Atomic shear strain and shear band development at different depths (indicated on the snapshots) during loading in 60°, 90°, and 120° nanoindentation.

generally align with one of these two directions. The direction closer to the indentation direction is called the lower shear band (LSB), and the other is called the upper shear band (USB). Fig. 6 shows that the activation of the shear band system is affected by the indenter angle, in which red arrows indicate activated shear bands and unactivated shear bands are indicated by blue arrows. As the indenter angle increases, less tensile hydrostatic stress builds up, but more extensive compressive stress builds up underneath the indenter, as seen in Fig. 3. From a sharp to a blunt indenter, a transition from the activation of the USB to the LSB is observed. While underneath the 90° indenter, both LSB and USB are activated. Under a blunter indenter, shear bands can be activated at a relatively shallower indentation depth, similar to what was observed in a previous study [45]. The circular plot in Fig. 6 shows the activation boundary for the USB and LSB under nanoindentation tests using different indenter angles. As seen in Fig. 4, the activated shear bands develop progressively along the preferred directions [46]. Significant

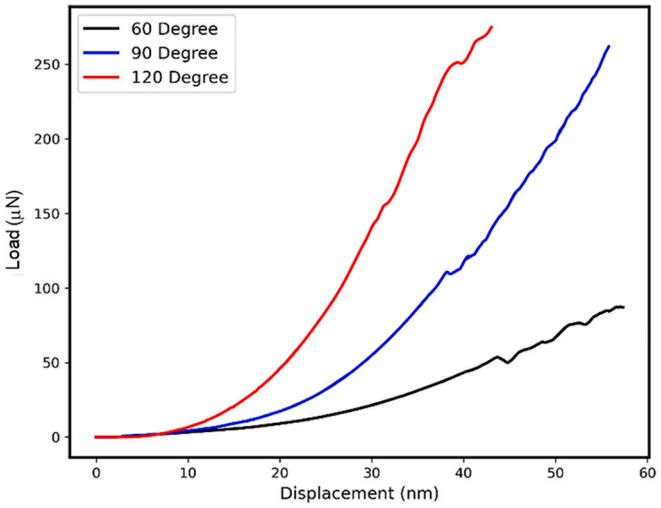

Fig. 5. Load-displacement curves during loading in 60°, 90°, and 120° nanoindentation.

structural rearrangements in glass are triggered when the shear bands reach the sample surface or interact with each other, which will be discussed in detail later by tracking undercoordinated atoms.

3-D nanoindentation allows a complete view of the shear deformation. As shown in Fig. 7, for the nanoindentation test using the 90° indenter, the shear bands have curved shapes, which are much more complex than the cross-section representations shown in previous studies [15,18,19,47]. Multiple shear bands interact with each other to form a complex plastic deformation zone, as seen in Fig. 4.

3.3. Undercoordinated atoms

Undercoordinated atoms with <60% nearest neighbors were tracked during nanoindentation tests to illustrate the structural changes, as shown in Fig. 8. For a sharp indenter of 60°, undercoordinated atoms appear near the indenter tip and propagate along the same direction as the USB toward the sample surface, resulting in push-up regions (marked by red rectangles) that are distinguishable from the commonly observed pile-up regions near the edges of the indenter in systems favoring shear deformation [5]. For a blunt indenter of 120°, undercoordinated atoms aggregate and propagate along the LSB direction, resulting in crack initiation at a certain distance below the indenter tip as the LSBs interact with each other and coalesce. The 90° nanoindentation is unique, where cracks initiate underneath and around the indenter and develop rapidly along the propagation directions of USB and LSB to form a complicated pattern. Fig. 8 clearly shows that the location of crack initiation and the direction of crack propagation are sensitively dependent on the indenter sharpness. However, a much larger sample size and much longer simulation time are needed to tell the resulting crack patterns. Interestingly, the surface push-up does not appear in the 90° and 120° nanoindentation tests in Fig. 8, which shows another strong effect of the indenter sharpness on the response of glass to sharp contact loading.

4. Discussion

4.1. Shear band activation and cavitation formation

Figs. 3 and 8 show that the crack initiates in the region where I_3 is positive. However, the interpretation of I_3 is not straightforward from Eq. 4. If I_3 is represented as the product of three principal stresses as below,

$$I_3 = \sigma_1\sigma_2\sigma_3 \tag{5}$$

then, I_3 is positive in regions where all three principal stresses are positive, or only the first principle stress is positive. Most of the positive I_3 regions fall into the second scenario, as shown in the Mohr's circle in Fig. 9. The principal stress can be as either tensile or compressive, and then the shear stresses can come from different combinations of principal stresses, in which the associated maximum shear stress τ_{12}^{max} is controlled by tensile stress σ_1 and compressive stress σ_2, τ_{23}^{max} is controlled by compressive stress σ_2 and σ_3, and the τ_{23}^{max} is controlled by tensile stress σ_1 and compressive stress σ_3. Figs. 10 and 11 show the

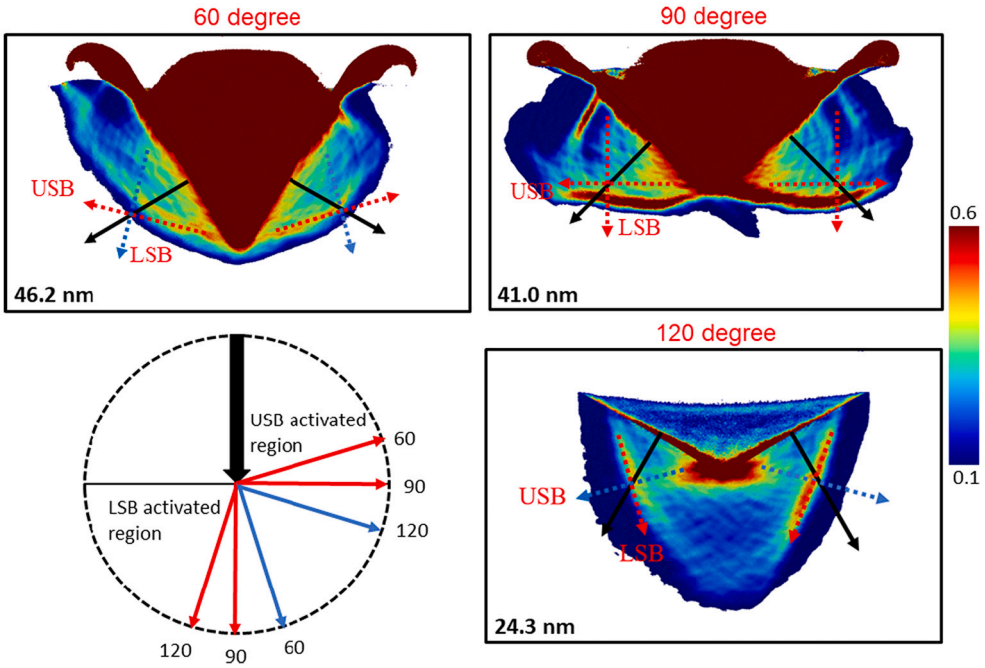

Fig. 6. Illustration of the development of the upper shear band system (USB) and the lower shear band system (LSB) during loading in 60°, 90°, and 120° nanoindentation at 46.2, 41.0, and 24.3 nm depth, respectively.

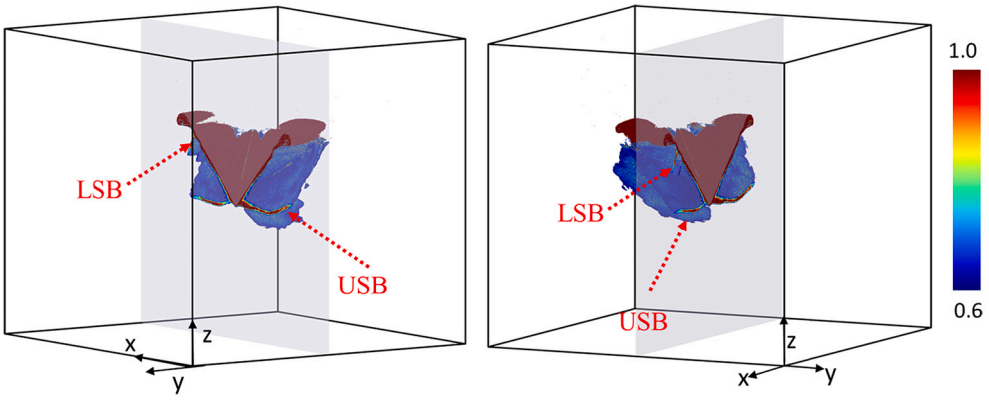

Fig. 7. Shear bands from different perspectives at 41.0 nm indentation depth during loading in 90° nanoindentation.

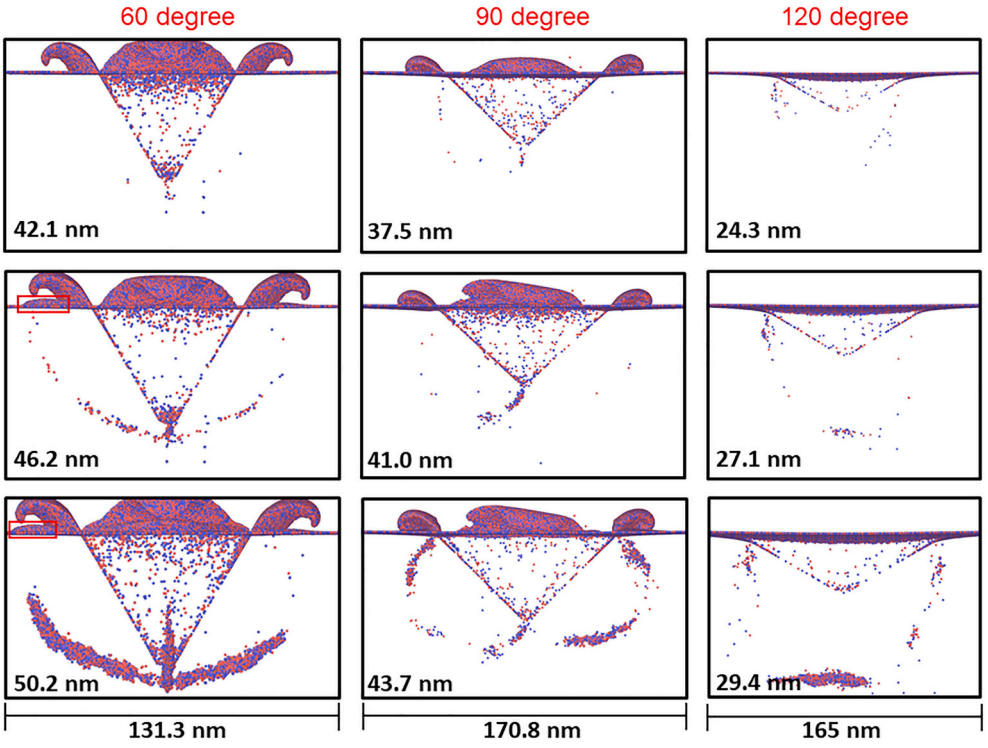

Fig. 8. Undercoordinated atoms at different indentation depths (indicated on snapshots) during loading in 60°, 90°, and 120° nanoindentation.

maximum shear stress components at different indentation depths during the shear band formation in 60° and 120° nanoindentation tests. It should be pointed out that the coordinate system for the principal stresses varies from point to point in the sample and is not aligned with the Cartesian coordinate system for the sample. For the 60° nanoindentation, τ_{23}^{max} and τ_{12}^{max} change significantly as the shear bands are activated while τ_{23}^{max} does not. For the 120° nanoindentation, τ_{23}^{max} and τ_{23}^{max} change significantly with the indentation depth while τ_{12}^{max} is very small and does not vary appreciably. Being the largest shear stress, τ_{23}^{max} has a significant effect on the shear band formation in both 60° to 120° nanoindentation tests. A switch from τ_{12}^{max} to τ_{23}^{max} playing a more active role is observed as the indenter angle change from 60° to 120°, which may explain the switch of the active shear band system from USB to LSB, as a larger area with a higher magnitude of compressive stress is seen under 120° nanoindentation in Fig. 3. Figs. 10 and 11 show that regardless of the shear band systems, the shear bands propagate toward the region where the shear stress level is high, and the shear stress is released in the region after the shear bands are activated. Furthermore,

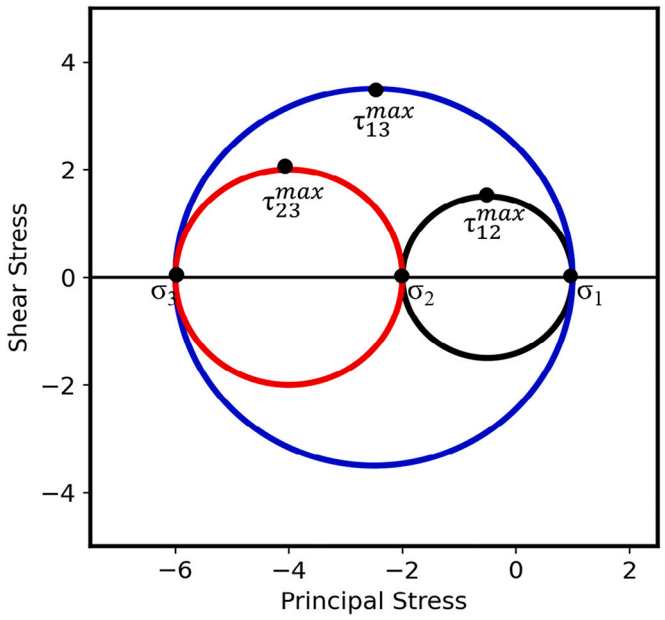

Fig. 9. Mohr's circles in the region where $\sigma_1 > 0$, σ_2 and $\sigma_3 < 0$ such that I_3 is positive.

the much larger τ_{12}^{max} in 60° than in 120° nanoindentation may explain the experimental observations that a shaper indenter promotes more shear deformation under indentation [30,33].

Similar to previous studies in metallic glasses, cavitations under the indenter originate in heavily deformed regions inside activated shear bands, where highly localized shear deformation weakens the structural stability [18,48–51]. The growth of cavitation is controlled by the shear band propagation direction, determined by the indenter sharpness, as shown in Fig. 6, and consistent with the observations in a previous study [43]. For a sharp indenter, the cavitation grows along with the USBs toward the sample surface, while for a blunt indenter, the cavitation grows where LSBs interact with each other underneath the indenter, as seen in Fig. 4. As recent experiments clearly showed that crack propagation in various glasses is dominated by the self-organized nucleation, growth, and coalescence of nanocavities [52], different cavitation sites under nanoindentation tests using different indenter angles will lead to different crack systems. Our simulations explain experimental observations that the indenter sharpness is an important controlling factor affecting the deformation and cracking behaviors of glass [9,30,33].

4.2. Temperature rise

Shear band formation is a thermomechanical process that initiates randomly as a self-catalytic process [53–57]. Temperature rise during the shear band formation process was widely observed, although it has been highly debated whether it is the cause or the consequence of the shear band formation [58–63]. Recently, a study in crystalline titanium showed some evidence that the stress peaks first, the shear band forms, and then the temperature rises [64]. However, the situation may be much more complicated in glass with complex stress and strain fields generated by indentation, as shown in Fig. 3 and Fig. 12. It was found that shear bands initiate in regions where atomic displacements point in different directions [55,57,65],. and the friction from the atomic motion in different directions generates significant heat, giving rise to temperature rise. Figs. 13 and 14 show that the temperature rise (333 K on average) in 60° nanoindentation is higher than that (167 K on average) in 120° nanoindentation during the shear band activation process but still much lower than the glass transition temperature of 900 K of the model metallic glass. This may be partially due to the fact that heat is being taken away by the thermostat at each time step during simulated nanoindentation tests. These results show that the indentation speed of 20 m/s used in this work, although high compared with experiments, is slow enough for the heat to be taken away efficiently, so the sample remains in the glass state.

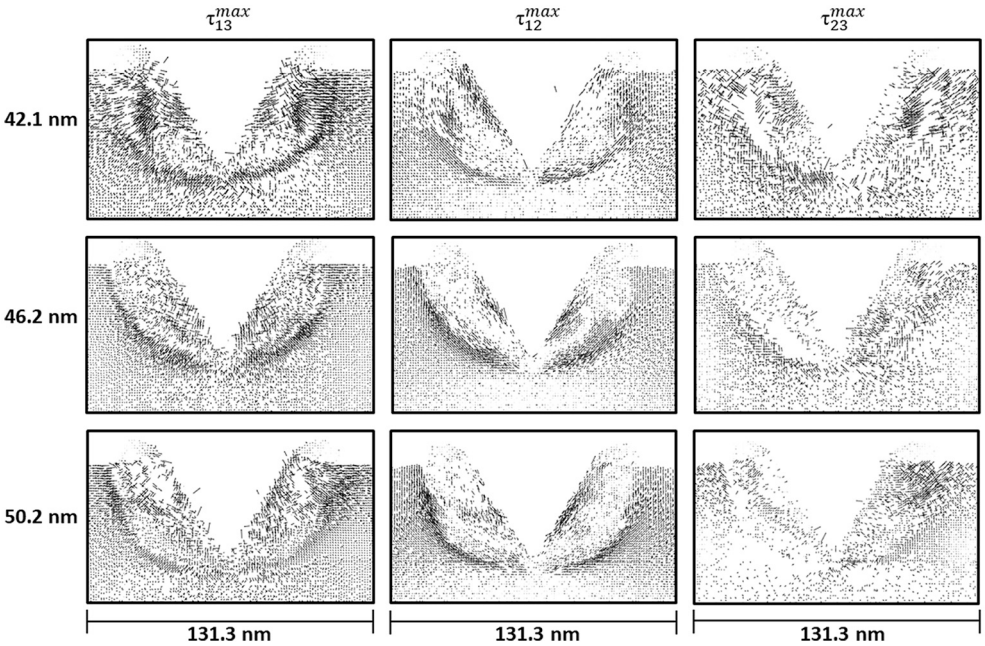

Fig. 10. Patterns of the maximum shear stress (represented by an arrow at each point to indicate the direction and magnitude) at different depths during loading in 60° nanoindentation.

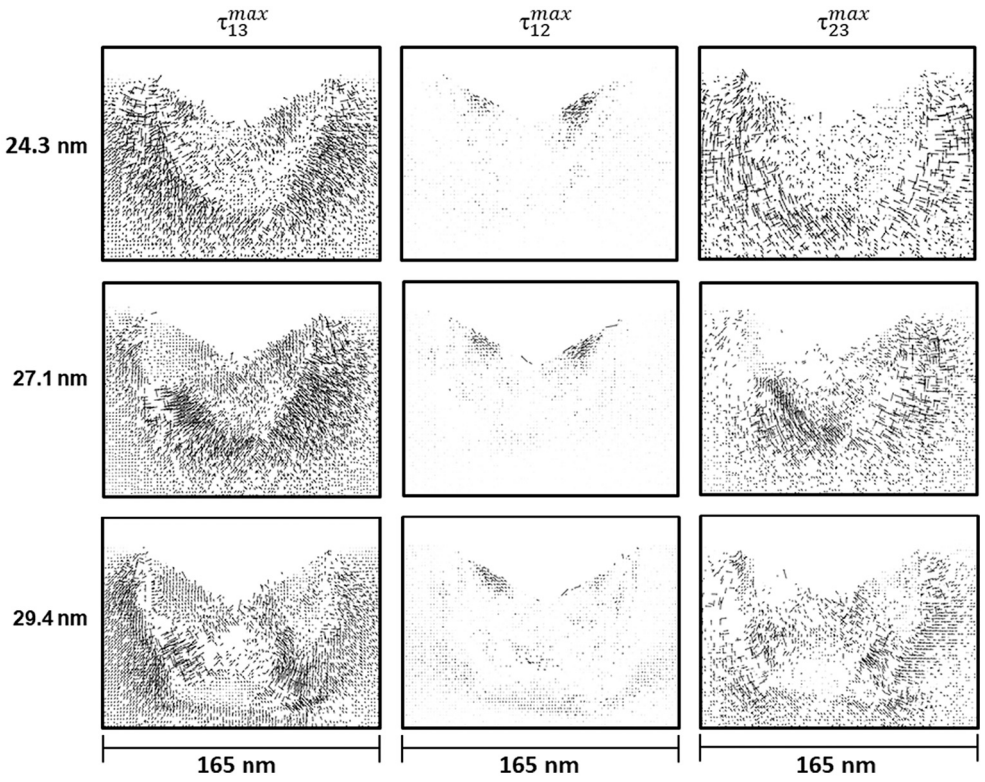

Fig. 11. Patterns of the maximum shear stress (represented by an arrow at each point to indicate the direction and magnitude) at different depths during loading in 120° nanoindentation.

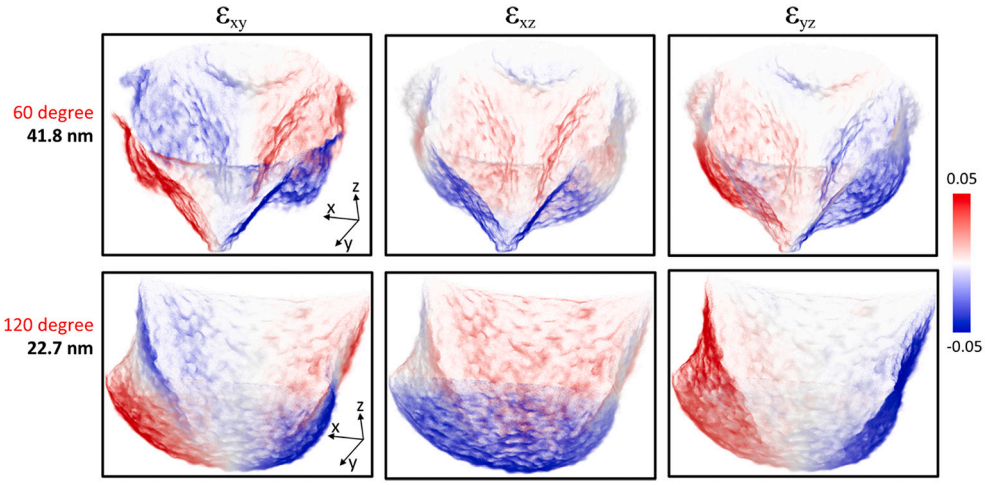

Fig. 12. Strain components before shear band activation in 60° and 120° nanoindentation.

4.3. Comparison with experiments

In a recent nanoindentation study using a cube-corner indenter in SLS glass, researchers found an inelastic deformation mode different from the pile-up near the sample surface, which was called lift-up and attributed to the lateral pushing of glass by the indenter [32]. The surface push-up in the 60° nanoindentation shown in Fig. 15(a) is similar to the lift-up observed in experiments in Fig. 15(b), but our simulations show that it is due to up movement of atoms associated with activated USBs. Under a blunter indenter of 120°, no surface push-up was observed as USBs were not activated. This is consistent with experimental observations that lift-up was only observed in

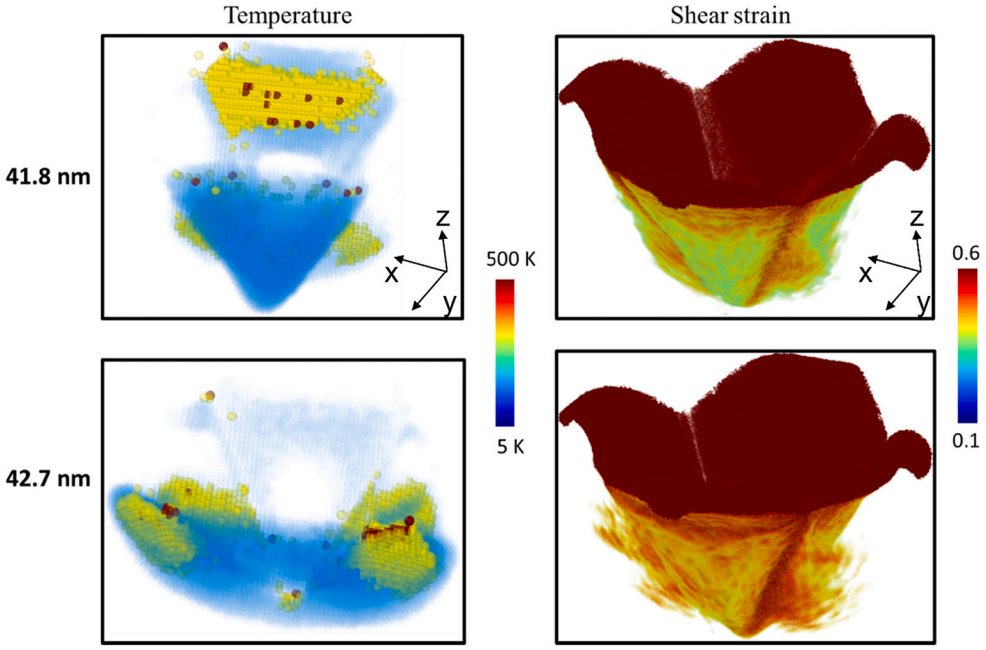

Fig. 13. Local temperature and shear strain during shear band activation in 60° nanoindentation. Transparency was used to render 3D representation clearer such that regions with temperature below 333 K or shear strain below 0.3 become invisible.

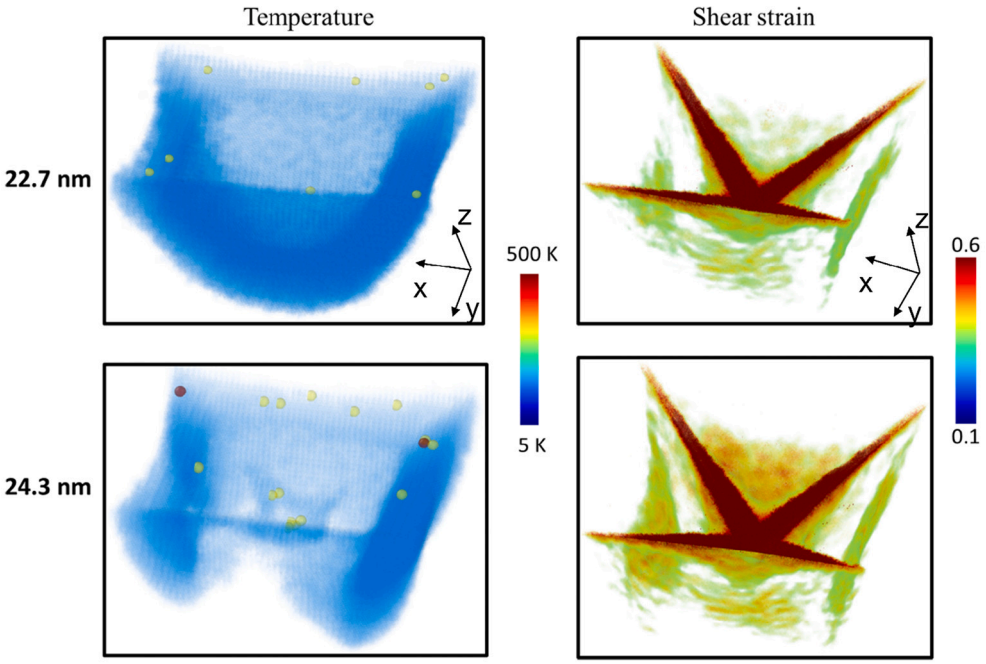

Fig. 14. Local temperature and shear strain during shear band activation in 120° nanoindentation. Transparency was used to render 3D representation clearer such that regions with temperature below 167 K or shear strain below 0.3 become invisible.

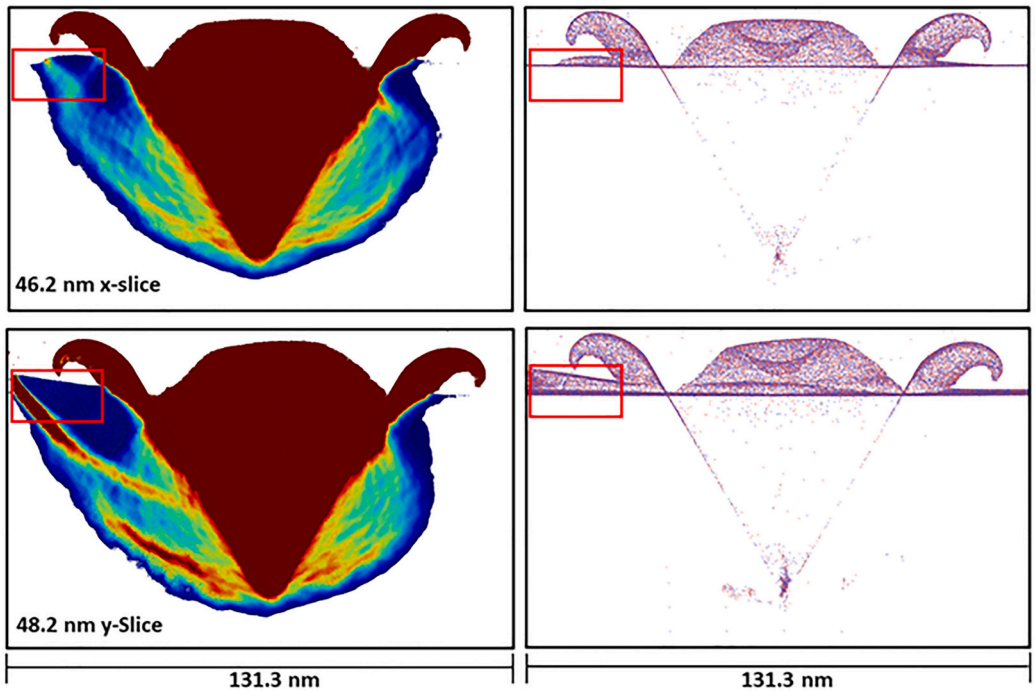

(a) Model metallic glass in MD simulations

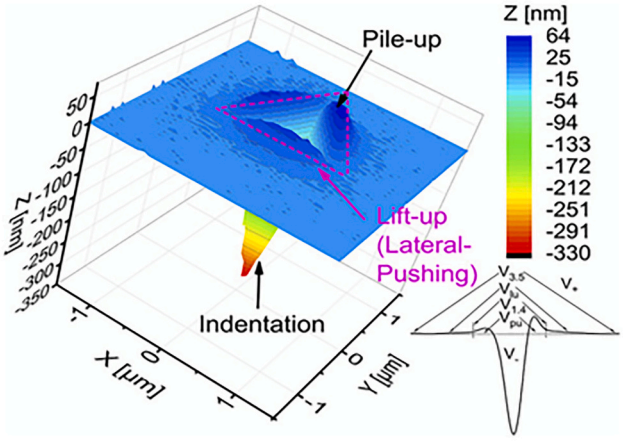

(b) SLS glass in experiments

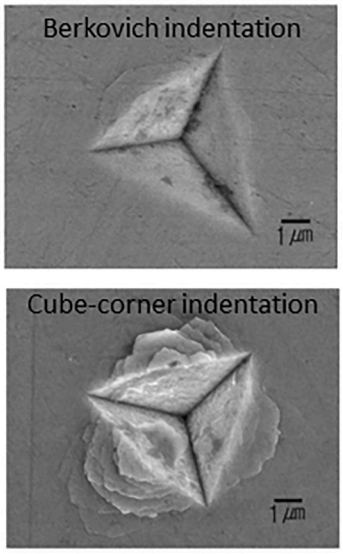

(c) Metallic glass in experiments

Fig. 15. (a) Surface push-up (highlighted by red rectangles) in model metallic glass from 60° nanoindentation in MD simulations, (b) lift-up (lateral pushing) in soda-lime silicate glass from cube-corner indentation in experiments [32], and (c) Berkovich indentation (without surface steps) and cube-corner indentation (with surface steps) in metallic glass in experiments [9]. ((b) and (c) were reproduced from Ref. 32 and 9 with permission.)

nanoindentation tests using a cube-corner indenter but was not seen when a Berkovich indenter was used as the former is sharper than the latter, as shown in Fig. 15(b). The surface push-up observed in the 60° nanoindentation may explain the surface steps observed around a cube-corner indent but not around a Berkovich indent in metallic glass in as seen Fig. 15(c) [9]. Although the surface push-up under a sharp indenter may look drastically different from the cavitation formation under a blunt indenter, and our simulation results show that they are both controlled by the activation of shear band systems moving in different directions.

The above-observed indenter sharpness effects can be understood based on the Sneddon's contact pressure distribution *P(r)* within a semi-infinite half-space loaded by a rigid conical indenter during elastic contact [9,12,33,66]:

$$P(r) = \frac{E}{2(1-\nu^2)} \frac{cosh^{-1}(a/r)}{tan\alpha} \quad (0 \le r \le a) \tag{6}$$

where E is the Young's modulus, ν is the Poisson's ratio, a is the contact radius, and r is the radial distance from the axis of the conical indenter, α is the semi-angle of the equivalent cone, which is 33.08, 48.45 and 62.90° for the 60, 90 and 120° pyramidal indenter to have the same projected area of indentation at a given depth, respectively. The Sneddon's contact pressure as a function of the radial distance of the

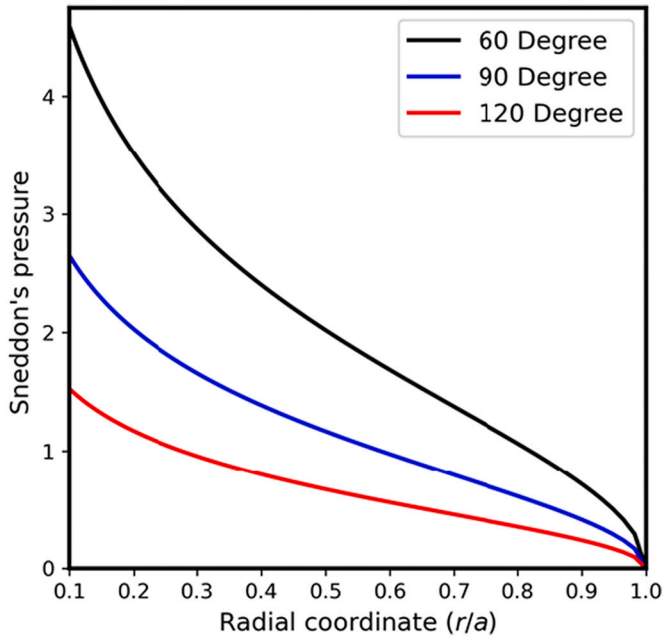

Fig. 16. Relation between Sneddon's contact pressure and radial distance from the axis of the equivalent conical indenter for the pyramidal indenter of 60°, 90°, and 120° used in this work.

equivalent cone for the three indenter angles used in this work are shown in Fig. 16. Since the E and ν are the same for all of the samples, only the geometric part of the Sneddon's contact pressure is plotted in Fig. 16, which shows that the contact pressure in the region near the indenter axis increases faster for a sharper indenter. The faster-rising contact pressure for a shaper contact angle agrees with the I_1 and I_3 patterns in Fig. 3. On the other hand, the maximum shear stress that plays an important role in plastic deformation and yielding can be given as [67]:

$$\tau_{\max} = \frac{P_m}{2(1+\alpha)} \tag{7}$$

where P_m is the mean contact pressure. Eq. 7 suggests that for the same mean contact pressure, a smaller cone semi-angle leads to a higher maximum shear stress, consistent with the observations in Figs. 10 and 11. Eqs. (6) and (7) show that a higher contact pressure, a higher maximum shear stress and a larger spatial distribution can be generated by a shaper indenter. So, for given critical stress required for shear bands formation and propagation, the probability that the shear bands can escape from under the contact to the sample surface is greater for a sharper indenter. This explains the observations in Fig. 15 that surface push-ups/lift-ups/steps are only observed in indentation using a sharp indenter.

Furthermore, we compared our simulation results of the model metallic glass with several experimental studies of SLS glass, which also favors the shear flow deformation under indentation [2,9,12,68–70]. As shown in Fig. 17, the pattern of LSBs and their interaction/coalescence in the 120° nanoindentation in MD look very similar to the shear bands and crack pattern found underneath a Vickers indenter (136°) in SLS glass [31]. Our simulation suggests that these shear bands and cracks form during the loading process. After unloading, the residual stress (indicated by birefringence) is localized in a circular region around the indent from the top view in SLS glass in experiments shown in Fig. 18(a), similar to the stress patterns from nanoindentation in model metallic glass in MD simulations in Fig. 18(b). Fig. 18(b) shows that the residual stress has both shear and hydrostatic components, and the residual hydrostatic tensile stress accumulates near the corners of the indenter, which would promote the radial crack formation during unloading as seen in experiments [68,71–73]. The above favorable comparisons with experimental results suggest that simulated 3-D nanoindentation tests can be a powerful tool for revealing deformation mechanisms of glass under sharp contact loading, despite the fact that the length and time scale accessible by MD simulations are significantly different from those in experiments.

5. Conclusions

A 3-D nanoindentation method in MD simulations was developed in this study to understand the deformation behaviors of a model metallic glass under sharp contact loading. Using this protocol, our simulated nanoindentation tests using different indenter angles reveal that the indenter sharpness plays a critical role in the shear band initiation, propagation, and interaction with each other that lead to cavitation and further damage in glass. For the first time, a surface push-up deformation mode due to the propagation of upper shear bands was observed in simulated nanoindentation tests using a sharp indenter. The surface push-up is a unique inelastic deformation mode that is distinct from the well-known pile-up phenomenon and should be taken into consideration

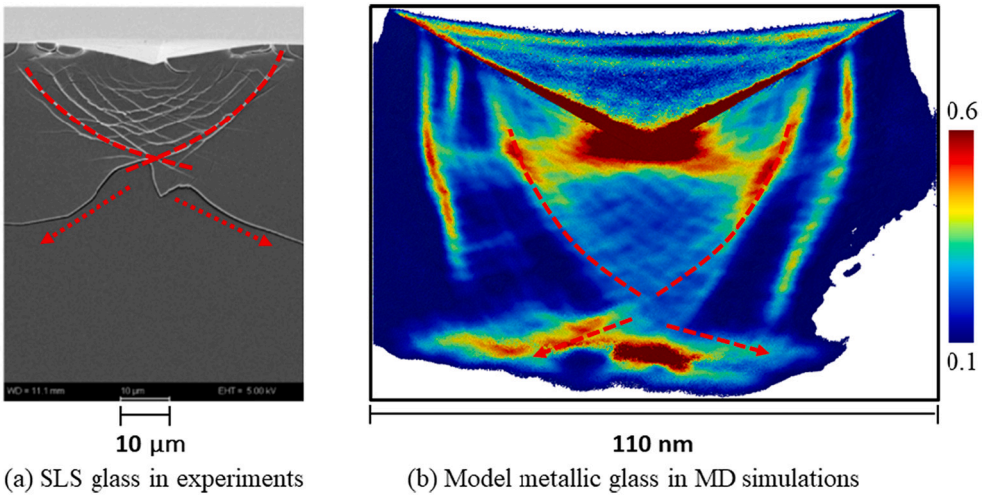

Fig. 17. Comparison between shear bands and crack pattern in (a) soda-lime silicate glass after Vickers indentation with 1 kgf in experiments (image taken after unloading) [31], and (b) model metallic glass from 120° nanoindentation during loading at an indentation depth of 29.4 nm in MD simulations. ((a) was reproduced from Ref. 31 with permission.)

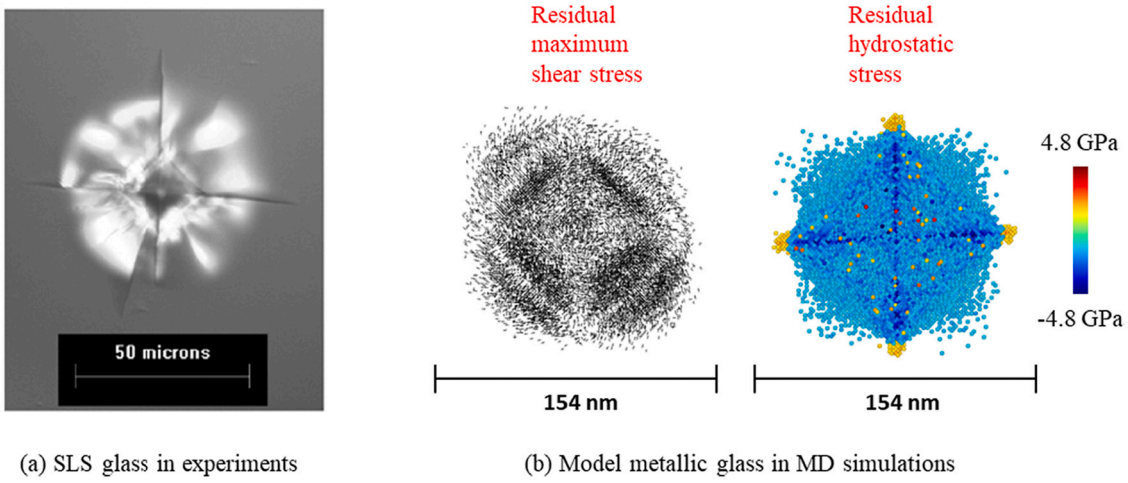

Fig. 18. Comparison between (a) optical birefringence pattern in soda-lime silicate glass from 120° pyramidal indentation after unloading from 200 gf in experiments [30], and (b) residual maximum shear stress (represented by an arrow at each point to indicate the direction and magnitude) and hydrostatic stress patterns in model binary metallic glass from 120° nanoindentation after unloading from 24.3 nm in MD simulations. ((a) was reproduced from Ref. 31 with permission.)

when a sharp indenter is used in instrumented indentation studies in experiments. By comparing our simulation results with multiple experimental studies in soda-lime silicate glass that deforms primarily via shear flow like the model metallic glass in this work, similar patterns of shear bands and residual stress fields were observed in these two glass systems. Our study demonstrates that simulated 3-D nanoindentation in MD simulations could serve as an essential tool to provide a complete understanding of deformation and cracking behaviors of glass in response to sharp contact loading, the first step toward the rational design of damage-resistant glasses for a wide range of applications.

Supplementary data to this article can be found online at https://doi.org/10.1016/j.nocx.2022.100130.

CRediT authorship contribution statement

Haidong Liu: Investigation, Formal analysis, Writing – original draft, Writing – review & editing. **Yunfeng Shi:** Conceptualization, Writing – review & editing. **Liping Huang:** Supervision, Funding acquisition, Conceptualization, Writing – review & editing.

Declaration of Competing Interest

The authors declare that they have no known competing financial interests or personal relationships that could have appeared to influence the work reported in this paper.

Data availability

Data will be made available on request.

Acknowledgments

This work was supported by the National Science Foundation under Grant No. DMR-1508410 and DMR-1936368. Computational resources from the Center for Computational Innovations (CCI) at RPI were used in performing the simulations.

References

[1] K. Januchta, M.M. Smedskjaer, J. Non-Cryst. Solids X 1 (2019), 100007.
[2] Proc. R. Soc. Lond. Ser. Math. Phys. Sci. 279 (1964) 420.
[3] J.T. Hagan, M.V. Swain, J. Phys. Appl. Phys. 11 (1978) 2091.
[4] F.M. Ernsberger, J. Am. Ceram. Soc. 51 (1968) 545.
[5] K.W. Peter, J. Non-Cryst. Solids 5 (1970) 103.
[6] A.K. Varshneya, Int. J. Appl. Glas. Sci. 9 (2018) 140.
[7] S. Yoshida, T.H. Nguyen, A. Yamada, J. Matsuoka, Mater. Trans. 60 (2019) 1428.
[8] E. Barthel, V. Keryvin, G. Rosales-Sosa, G. Kermouche, Acta Mater. 194 (2020) 473.
[9] B.-G. Yoo, J.-Y. Kim, J. Jang, Mater. Trans. 48 (2007) 1765.
[10] K.P. Marimuthu, K. Lee, J. Han, F. Rickhey, H. Lee, J. Mater. Res. Technol. 9 (2020) 104.
[11] C.A. Schuh, T.G. Nieh, Acta Mater. 51 (2003) 87.
[12] H. Huang, H. Zhao, Mater. Trans. 55 (2014) 1400.
[13] C.R. Kurkjian, S.M. Allameh, S. Yoshida, Int. J. Appl. Glas. Sci. 13 (2022) 11.
[14] Y.B. Gerbig, C.A. Michaels, J. Non-Cryst. Solids 530 (2020), 119828.
[15] Y. Shi, M.L. Falk, Acta Mater. 55 (2007) 4317.
[16] Y. Shi, J. Luo, F. Yuan, L. Huang, J. Appl. Phys. 115 (2014), 043528.
[17] F. Yuan, L. Huang, Sci. Rep. 4 (2015) 5035.
[18] Y. Yang, J. Luo, L. Huang, G. Hu, K.D. Vargheese, Y. Shi, J.C. Mauro, Acta Mater. 115 (2016) 413.
[19] K.-H. Lee, Y. Yang, J.C. Mauro, J. Appl. Phys. 125 (2019), 025106.
[20] H. Liu, B. Deng, S. Sundararaman, Y. Shi, L. Huang, J. Appl. Phys. 128 (2020), 035106.
[21] D. Zhao, B. Zhu, S. Wang, Y. Niu, L. Xu, H. Zhao, Comput. Mater. Sci. 186 (2021), 110073.
[22] S. Urata, Y. Sato, J. Chem. Phys. 147 (2017), 174501.
[23] J. Luo, K.D. Vargheese, A. Tandia, G. Hu, J.C. Mauro, Sci. Rep. 6 (2016) 23720.
[24] S. Urata, Y. Takato, K. Maeda, J. Am. Ceram. Soc. 102 (2019) 5138.
[25] D.A. Kilymis, J.M. Delaye, J. Non-Cryst. Solids 382 (2013) 87.
[26] D.A. Kilymis, J.-M. Delaye, J. Non-Cryst. Solids 401 (2014) 147.
[27] D.A. Kilymis, J.-M. Delaye, S. Ispas, J. Chem. Phys. 145 (2016), 044505.
[28] K. Nomura, Y.-C. Chen, R.K. Kalia, A. Nakano, P. Vashishta, Appl. Phys. Lett. 99 (2011), 111906.
[29] Y. Shi, Int. J. Appl. Glas. Sci. 7 (2016) 464.
[30] T.M. Gross, J. Non-Cryst. Solids 358 (2012) 3445.
[31] T.M. Gross, J. Wu, D.E. Baker, J.J. Price, R. Yongsunthon, J. Non-Cryst. Solids 494 (2018) 13.
[32] L. Ding, Y. Xu, R. Yang, Y. Yang, R. Lu, H. Liu, H. He, Q. Zheng, J.C. Mauro, J. Am. Ceram. Soc. 105 (2022) 2625.
[33] S. Yoshida, H. Sawasato, T. Sugawara, Y. Miura, J. Matsuoka, J. Mater. Res. 25 (2010) 2203.
[34] H. Carter Edwards, C.R. Trott, D. Sunderland, J. Parallel Distrib. Comput. 74 (2014) 3202.
[35] S. Plimpton, J. Comput. Phys. 117 (1995) 1.
[36] S. Melchionna, G. Ciccotti, B. Lee Holian, Mol. Phys. 78 (1993) 533.
[37] D.A. Kilymis, J.-M. Delaye, J. Chem. Phys. 141 (2014), 014504.
[38] J.F. Ziegler, J.P. Biersack, in: D.A. Bromley (Ed.), Treatise Heavy-Ion Sci, Springer, US, Boston, MA, 1985, pp. 93–129.
[39] O.C. Zienkiewicz, R.L. Taylor, D. Fox, in: O.C. Zienkiewicz, R.L. Taylor, D. Fox (Eds.), Finite Elem. Method Solid Struct. Mech, Seventh ed., Butterworth-Heinemann, Oxford, 2014, pp. 75–145.
[40] J. Luo, P.J. Lezzi, K.D. Vargheese, A. Tandia, J.T. Harris, T.M. Gross, J.C. Mauro, Front. Mater. 3 (2016).
[41] J. Luo, K.D. Vargheese, A. Tandia, J.T. Harris, J.C. Mauro, J. Non-Cryst. Solids 452 (2016) 297.
[42] T. Rouxel, J. Jang, U. Ramamurty, Prog. Mater. Sci. 121 (2021), 100834.
[43] J.L. Bucaille, S. Stauss, E. Felder, J. Michler, Acta Mater. 51 (2003) 1663.
[44] L. Krämer, V. Maier-Kiener, Y. Champion, B. Sarac, R. Pippan, Mater. Des. 155 (2018) 116.
[45] H. Zhang, S. Maiti, G. Subhash, J. Mech. Phys. Solids 56 (2008) 2171.
[46] M.Q. Jiang, L.H. Dai, Acta Mater. 59 (2011) 4525.
[47] A.J. Cao, Y.Q. Cheng, E. Ma, Acta Mater. 57 (2009) 5146.
[48] M.H. Cohen, D. Turnbull, J. Chem. Phys. 31 (1959) 1164.

[49] H.J. Leamy, T.T. Wang, H.S. Chen, Metall. Mater. Trans. B Process Metall. Mater. Process. Sci. 3 (1972) 699.
[50] R. Maaß, P. Birckigt, C. Borchers, K. Samwer, C.A. Volkert, Acta Mater. 98 (2015) 94.
[51] D. Klaumünzer, A. Lazarev, R. Maaß, F.H. Dalla Torre, A. Vinogradov, J.F. Löffler, Phys. Rev. Lett. 107 (2011), 185502.
[52] L.-Q. Shen, J.-H. Yu, X.-C. Tang, B.-A. Sun, Y.-H. Liu, H.-Y. Bai, W.-H. Wang, Sci. Adv. 7 (2021) eabf7293.
[53] J.S. Langer, Scr. Mater. 54 (2006) 375.
[54] R. Maaß, J.F. Löffler, Adv. Funct. Mater. 25 (2015) 2353.
[55] D. Şopu, A. Stukowski, M. Stoica, S. Scudino, Phys. Rev. Lett. 119 (2017), 195503.
[56] M.L. Falk, J.S. Langer, Phys. Rev. E 57 (1998) 7192.
[57] Z.-Y. Yang, Y.-J. Wang, L.-H. Dai, Phys. Rev. Res. 4 (2022), 023220.
[58] C. Zener, J.H. Hollomon, J. Appl. Phys. 15 (1944) 22.
[59] Y.L. Bai, J. Mech. Phys. Solids 30 (1982) 195.
[60] T.W. Wright, R.C. Batra, Int. J. Plast. 1 (1985) 205.
[61] R.C. Batra, C.H. Kim, Int. J. Plast. 6 (1990) 127.
[62] M.A. Meyers, Y.B. Xu, Q. Xue, M.T. Pérez-Prado, T.R. McNelley, Acta Mater. 51 (2003) 1307.
[63] E.K. Cerreta, J.F. Bingert, G.T. Gray, C.P. Trujillo, M.F. Lopez, C.A. Bronkhorst, B. L. Hansen, Int. J. Plast. 40 (2013) 23.
[64] Y. Guo, Q. Ruan, S. Zhu, Q. Wei, H. Chen, J. Lu, B. Hu, X. Wu, Y. Li, D. Fang, Phys. Rev. Lett. 122 (2019), 015503.
[65] O. Gendelman, P.K. Jaiswal, I. Procaccia, B.S. Gupta, J. Zylberg, EPL Europhys. Lett. 109 (2015) 16002.
[66] I.N. Sneddon, Int. J. Eng. Sci. 3 (1965) 47.
[67] R. Hill, E.H. Lee, S.J. Tupper, N.F. Mott, Proc. R. Soc. Lond. Ser. Math. Phys. Sci. 188 (1947) 273.
[68] A. Arora, D.B. Marshall, B.R. Lawn, M.V. Swain, J. Non-Cryst. Solids 31 (1979) 415.
[69] J.T. Hagan, S. Van Der Zwaag, J. Non-Cryst. Solids 64 (1984) 249.
[70] T. Rouxel, H. Ji, J.P. Guin, F. Augereau, B. Rufflé, J. Appl. Phys. 107 (2010), 094903.
[71] R.F. Cook, G.M. Pharr, J. Am. Ceram. Soc. 73 (1990) 787.
[72] D.B. Marshall, B.R. Lawn, J. Mater. Sci. 14 (1979) 2001.
[73] B.R. Lawn, T.P. Dabbs, C.J. Fairbanks, J. Mater. Sci. 18 (1983) 2785.